



Revealing *OOH key intermediates and regulating H₂O₂ photoactivation by surface relaxation of Fenton-like catalysts

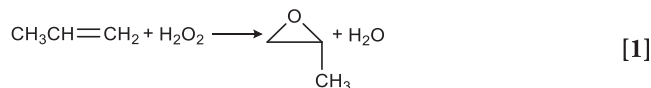
Xiaoming Xu^{a,b}, Yuanming Zhang^{a,b}, Yong Chen^{a,b}, Changhao Liu^{a,b}, Wenjing Wang^{a,b}, Jijia Wang^c, Huiting Huang^{a,b}, Jianyong Feng^{a,b}, Zhaosheng Li^{a,b,1}, and Zhigang Zou^{a,b}

Edited by Alexis Bell, University of California, Berkeley, CA; received March 30, 2022; accepted July 8, 2022

Hydrogen peroxide (H₂O₂) molecules play important roles in many green chemical reactions. However, the high activation energy limits their application efficiency, and there is still huge controversy about the activation path of H₂O₂ molecules over the presence of *OOH intermediates. Here, we confirmed the formation of the key species *OOH in the heterogeneous system, via in situ shell-isolated nanoparticle-enhanced Raman spectroscopy (SHINERS), isotope labeling, and theoretical calculation. In addition, we found that compared with *H₂O₂, *OOH was more conducive to the charge transfer behavior with the catalyst and the activation of an O-O bond. Furthermore, we proposed to improve the local coordination structure and electronic density of the YFeO₃ catalyst by regulating the surface relaxation with Ti modification so as to reduce the activation barrier of H₂O₂ and to improve the production efficiency of •OH. As a result, the kinetics rates of the Fenton-like (photo-Fenton) reaction had been significantly increased several times. The •OH free radical activity mechanism and molecular transformation pathways of 4-chloro phenol (4-CP) were also revealed. This may provide a clearer vision for the further study of H₂O₂ activation and suggest a means of designing catalysts for efficient H₂O₂ activation.

photoactivation | H₂O₂ | surface relaxation | *OOH species | Fenton-like process

Hydrogen peroxide (H₂O₂), as a high-value green compound (1, 2), has a wide range of applications in bleaching, environmental purification, green chemicals, food, medicine, military, and other fields. Especially, in the reactions of green organic industrial synthesis, pollutant removal, such as the green preparation of propylene derivatives (Eq. 1) and the synthesis of epoxy resin monomers (Eq. 2), H₂O₂ molecules play an irreplaceable role as a significant oxidant (3–7):



In those reactions, the real active species are mainly some free radicals from the decomposition of H₂O₂ molecules (8–12). However, because H₂O₂ molecules own relatively high activation energy, the reaction kinetics is generally limited, which has become a bottleneck for the development of those reactions (4, 13–15). In order to improve the activation of H₂O₂ molecules, many studies have extended the homogeneous reaction system to the heterogeneous system (16, 17). The activation of H₂O₂ molecules can be further improved by the catalyst to stimulate the H₂O₂ molecules. Among them, the heterogeneous Fenton-like reaction is an extremely classic system that has been widely studied (18–21).

In order to promote the activation of H₂O₂ molecules, some efficient strategies have been used (22–24), such as single atom modification, defect engineering, heterogeneous engineering, and facet engineering. The single-atom Cr-N₄ sites at pyrrolic N-rich g-C₃N₄ may act as the peroxidase mimicking nanozymes, which efficiently activate H₂O₂ to produce •OH (22). Zhan et al. (23) prepared a defect-engineered iron single-atom photocatalyst to regulate the local electron density of the Fe single sites, promoting the activation of H₂O₂ molecules. Xing et al. (24) designed a CoFe₂O₄/MoS₂ heterogeneous Fenton system to accelerate the circulation of Fe³⁺/Fe²⁺, further activating the decomposition of H₂O₂ molecules.



Significance

Hydrogen peroxide (H₂O₂), as a green oxidant, has important application value in sewage treatment and green chemical synthesis. However, it is usually limited by a relatively high activation energy, and its activation path in heterogeneous systems has always been controversial. Assessments using shell-isolated nanoparticle-enhanced Raman spectroscopy (SHINERS), isotope labeling, and theoretical calculations confirmed the construction of key species *OOH to distinguish the controversial paths. Moreover, we proposed a strategy to promote H₂O₂ activation, which could promote the stretching of H₂O₂ molecules and the charge transfer behavior with catalysts by regulating the surface relaxation of catalysts. This provided insights for an in-depth understanding of the H₂O₂ molecular activation mechanism and its more efficient utilization.

Author contributions: Z.L. and X.X. designed research; X.X., Y.Z., Y.C., C.L. and W.W. performed research; X.X., Y.Z., J.W., H.H., J.F. and Z.L. analyzed data; X.X., Z.L. and Z.Z. wrote the paper. All authors contributed to the discussions of the results in this manuscript.

The authors declare no competing interest.

This article is a PNAS Direct Submission.

Copyright © 2022 the Author(s). Published by PNAS. This article is distributed under Creative Commons Attribution-NonCommercial-NoDerivatives License 4.0 (CC BY-NC-ND).

¹To whom correspondence may be addressed. Email: zsl@nju.edu.cn.

This article contains supporting information online at <http://www.pnas.org/lookup/suppl/doi:10.1073/pnas.2205562119/-/DCSupplemental>.

Published August 29, 2022.

Crucially, the way that H_2O_2 decomposes to produce active species is still a huge controversy. In many studies, the decomposition path of H_2O_2 was the breaking of the O-O bond, resulting in two $\cdot\text{OH}$ groups (Eq. 3) (25–27). Nevertheless, there was another mechanism by which the decomposition of H_2O_2 molecules might have caused O-H bond cleavage to produce $\cdot\text{OOH}$ species and then have caused O-O cleavage to produce $\bullet\text{OH}$ radicals (Eq. 4) (28–30). For Eq. 4, the reported works were mainly speculative and there was lack of direct experimental evidence for the formation of $\cdot\text{OOH}$. The core species that distinguished these two paths were the $\cdot\text{OOH}$ species. However, the survival time of these intermediate species was extremely short, and they mainly existed at the solid-liquid interface; thus, they were very difficult to be tracked and detected. Shell-isolated nanoparticle-enhanced Raman spectroscopy (SHINERS) (31–33) can enhance the signal of species adsorbed on the catalyst surface by 10^7 to 10^8 times, which provided infinite possibility for detecting these intermediate species. If these species can be traced, it will be of great significance for deepening the understanding of the catalytic reaction with H_2O_2 as the active substance. In order to further discuss the problem of molecular activation, we used the heterogeneous Fenton-like reaction as a model to conduct a more in-depth study.

In this study, a narrow-band, flexible, perovskite-type hexagonal YFeO_3 catalyst (34, 35) was used as the model catalyst. Combined with SHINERS and isotope labeling, we studied the process of H_2O_2 molecule transformation on the catalyst surface and confirmed the existence of $\cdot\text{OOH}$ species in a heterogeneous system. In addition, the density functional theory (DFT) results indicated that the formation of $\cdot\text{H-OOH}$ (TS) species in the decomposition process of H_2O_2 was easier than that of $\cdot\text{HO-OH}$ (TS), verifying the consequence of SHINERS. Furthermore, we proposed an efficient strategy to improve the photoactivation of H_2O_2 molecules. We found that regulating the surface relaxation of catalysts by Ti modification can make changes in the local coordination environment (bond length, atomic space, and coordination number) of YFeO_3 catalysts. These changes can promote the activation of H_2O_2 molecules and the production of $\cdot\text{OOH}$ species. In the Fenton-like reaction, a Ti-doped YFeO_3 catalyst was found significantly to improve the generation of active radicals and the removal rate of pollutants, compared to pure YFeO_3 . This provided a perspective for understanding the photoactivation mechanism of H_2O_2 molecules.

Results

Detection of Intermediate Species by SHINERS. The YFeO_3 catalysts were obtained by a sol-gel method (*SI Appendix, Fig. S1*). A comprehensive characterization of the catalysts was shown in *SI Appendix, Figs. S2–S9*. All the characteristic peaks of YFeO_3 agreed well with those of the standard card for YFeO_3 (Joint Committee on Powder Diffraction Standards (JCPDS) No. 48-0529; Fig. 1*A*). The microstructures of YFeO_3 were studied by spherical aberration-corrected scanning transmission electron microscopy (STEM) combined with high-angle annular dark field (HAADF), annular bright field (ABF), and the theoretical crystal structure. The HAADF (Fig. 1*B*) and ABF (*SI Appendix, Fig. S9A*) images and corresponding fast Fourier transform patterns (Fig. 1*B*) clearly demonstrated that the obtained YFeO_3 materials had the regularity of atomic arrangement, which correspond to the hexagonal phase. As shown in Fig. 1*B*, the brightness profile along the yellow lines clearly showed the distribution of the Y atoms.

In order to study the mechanism of H_2O_2 molecular activation, we conducted a series of in situ SHINERS, isotope labeling measurements, and theoretical calculations. For the study of these key intermediate species, we mainly focused on the interaction between H_2O_2 molecules and the catalysts. The SHINERS used in this experiment had Au@SiO_2 shell-isolated nanoparticles (SHINs; Au nanoparticles were ~ 45 nm coated with 2-nm SiO_2 layers) (Fig. 1*C*), which were evenly dispersed on the surface of the YFeO_3 particle-assembled film. As the passivation layer of Au particles, SiO_2 can avoid the interaction between Au particles and reactive species (32). Fig. 1*D* showed that under the irradiation of this laser, the catalyst- H_2O_2 system simulated the process of the Fenton-like (photo-Fenton) reaction, and the produced intermediate species were also detected by in situ SHINERS.

Then, a series of comparative tests were performed to fully study the intermediate process of the reaction between the YFeO_3 catalyst and H_2O_2 molecules (Fig. 1*E*). The peak around 874 cm^{-1} in our experiment was assigned to the O-O stretching vibration of H_2O_2 species (36). Only in the SHINs- YFeO_3 - H_2O_2 system, there occurred three obvious Raman peaks around 563 , 632 , and $1,091\text{ cm}^{-1}$. The experience of SHINs- YFeO_3 - H_2O , isotope labeling D_2O and H_2^{18}O had no signal (Fig. 1*F*), which eliminated the possibility that the above three enhanced signals may be derived from the action of water with catalysts. These three Raman vibration signals come from intermediate species produced during the decomposition of H_2O_2 . The O-O bond vibration characteristics of $\text{H}_2^{18}\text{O}_2$ were clearly detected around 828 cm^{-1} in the Raman spectra (*SI Appendix, Fig. S10*). The signal had a 46-cm^{-1} red shift, which matched the shift of -45 cm^{-1} predicted by Hooke's law for a diatomic O-O stretch. In addition, as shown in Fig. 1*E*, no signal of $\cdot\text{OOH}$ was detected in the SHINs- H_2O_2 system, which also proved that SHINs did not have the ability to activate H_2O_2 molecules and the activation of H_2O_2 molecules was attributed to the YFeO_3 catalyst. The peak around 563 cm^{-1} in our experiment was assigned to the Fe-O stretching vibration of Fe-OH species (37). The peak around 632 cm^{-1} was assigned to the Fe-O stretching vibration of Fe-OOH species (38, 39). And the peak around $1,091\text{ cm}^{-1}$ was assigned to Fe-O_2^- species (40). To further confirm this consequence, the DFT method was also employed to calculate the vibrational frequencies of $\cdot\text{OOH}$ species at the YFeO_3 surface. The calculated consequence showed that the correlated Raman frequencies of the Fe-O stretching vibration for Fe-OOH species was $\sim 638\text{ cm}^{-1}$ (Fig. 1*G*), which was consistent with our measured results. Therefore, we confirmed the existence of the H_2O_2 decomposition pathway with $\cdot\text{OOH}$ as the intermediate product. Its signal strength was stronger than that of $\cdot\text{OH}$, indicating that this pathway may play a leading role in the H_2O_2 decomposition process. The results of a set of simulated Fenton-like processes performed over time detected by in situ SHINERS were shown in Fig. 1*H*. As the time increased, all signals of Fe-OOH and Fe-OH decreased, which proved their strong correlation with H_2O_2 . Fig. 1*I* showed their possible formation process. H_2O_2 molecules were adsorbed by a single oxygen adsorption mode with YFeO_3 . Along with the process of deprotonation, Fe-OOH species were formed and there would occur the electron transfer process (the red point represented e^-) between the catalyst and $\cdot\text{OOH}$. These electrons mainly came from photogenerated electrons formed by semiconductor under photon excitation. Then, they converted to $\bullet\text{OH}$ species after charge transfer and the O-O bonds breaking.

Advantages of $\cdot\text{OOH}$ and Ideas for Regulating Its Activation.

In the process of $\cdot\text{OOH}$ activation to form $\bullet\text{OH}$, charge transfer occurs between $\cdot\text{OOH}$ and the catalyst through Fe-O bonds.

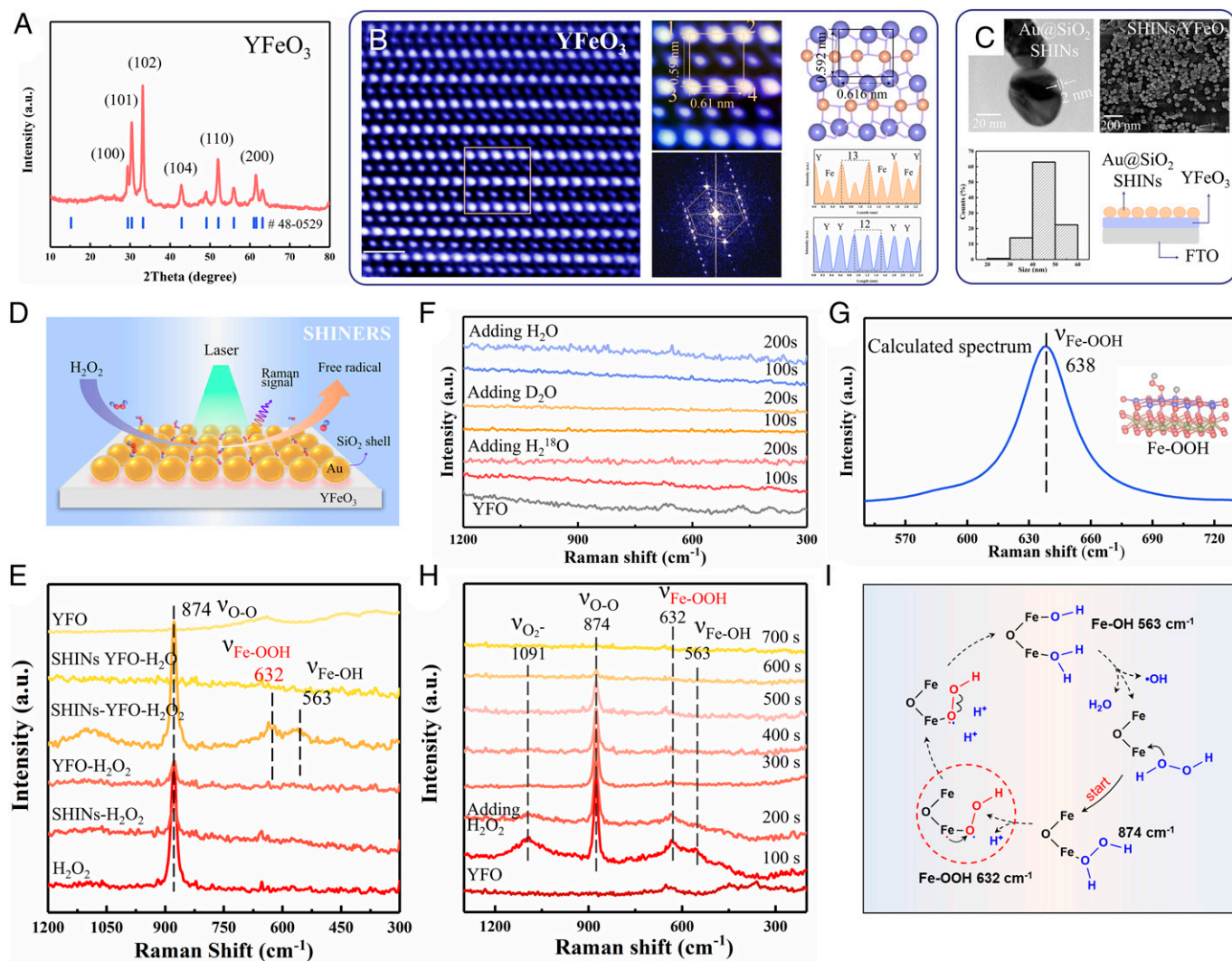


Fig. 1. In situ SHINERS, calculated spectrum, and possible mechanism. (A) XRD patterns of YFeO_3 . (B) HAADF image of YFeO_3 . The scale bar is 1 nm. (C) TEM image of Au@SiO_2 SHINs. SEM image of YFeO_3 catalysts modified with SHINs, and size distribution of SHINs nanoparticles. (D) Schematic of SHINERS detection of photo-Fenton process. (E) SHINERS spectra in different systems. (F) SHINERS spectra of isotope labeling. (G) The correlated Raman frequencies of the Fe-O stretching vibration for Fe-OOH species (gray; H; red, O; blue, Fe; yellow, Y). (H) SHINERS spectra of in situ reaction in the decomposition process of H_2O_2 as a function of time. (I) The possible mechanism for the activation process of H_2O_2 .

This process was a key stage in the evolution of H_2O_2 . The traditional adsorption configuration showed that the charge transfer formed at Fe-O_{a1} and Fe-O_{a2} sites was very close (Fig. 2A). With $^*\text{OOH}$ as the intermediate species, Fe-O_{b1} obtained more charges, making the suspended oxygen (O_{b2}) form an electron-deficient state (Fig. 2B). If YFeO_3 was modified by Ti doping (named Ti- YFeO_3), it may cause the change of local charge density and coordination structure of Fe sites. As shown in Fig. 2C, Fe-O_{c1} will obtain more charge than Fe-O_{a1} and Fe-O_{b1} . In the activation process, one oxygen of both $^*\text{OOH}$ and $^*\text{H}_2\text{O}_2$ tended to obtain electrons, while the other oxygen formed electron-deficient $\bullet\text{OH}$ species (Fig. 2D). Therefore, when the external charge was injected into $^*\text{OOH}$ species through an Fe-O bond, more favorable charge transfer and distribution would be formed quickly for $\text{YFeO}_3\text{-OOH}$ than $\text{YFeO}_3\text{-H}_2\text{O}_2$. O_{b1} was easier to form O^{2-} , while O_{b2} was easier to form electron-deficient $\bullet\text{OH}$. This indicated that taking $^*\text{OOH}$ as the intermediate species was more conducive to the charge transfer process with the catalyst. Moreover, compared with $\text{YFeO}_3\text{-OOH}$, Ti- $\text{YFeO}_3\text{-OOH}$ is more favorable for the above electron transfer process. Furthermore, the crystal orbital Hamilton populations (COHP) of $^*\text{OOH}$ adsorbed on YFeO_3 and Ti- YFeO_3 (Ti-doped

YFeO_3) were calculated (Fig. 2E and F). Integral crystal orbital Hamilton populations (ICOHP) results (Fig. 2G) showed that the intensity of the O-O bond from $^*\text{OOH}$ adsorbed on Ti- YFeO_3 (ICOHP = 2.37/2.48) was weaker than that on YFeO_3 (ICOHP = 3.50/3.53). The O-O bond of $^*\text{OOH}$ on Ti- YFeO_3 was easier to break and form $\bullet\text{OH}$. These charge transfer behavior and chemical bond activation calculation results provided a theoretical basis for the design of catalysts for efficient activation of H_2O_2 .

Surface Relaxation of Catalysts. To complement the above theoretical study, we sought to design Ti-doped YFeO_3 catalysts by a sol-gel method. All the characteristic peaks of obtained Ti-doped YFeO_3 agreed well with those of the standard card for YFeO_3 . The X-ray diffraction pattern (XRD), transmission electron microscopy (TEM), X-ray photoelectron spectroscopy (XPS), Brunauer-Emmett-Teller (BET) surface area images, STEM images, and other characterization results were shown in *SI Appendix, Figs. S2–S9*. Among the catalysts with different doping ratios, we chose 3% Ti-doped YFeO_3 as a typical one for further study, which was referred to as Ti- YFeO_3 . Especially, after modification with Ti, the existence

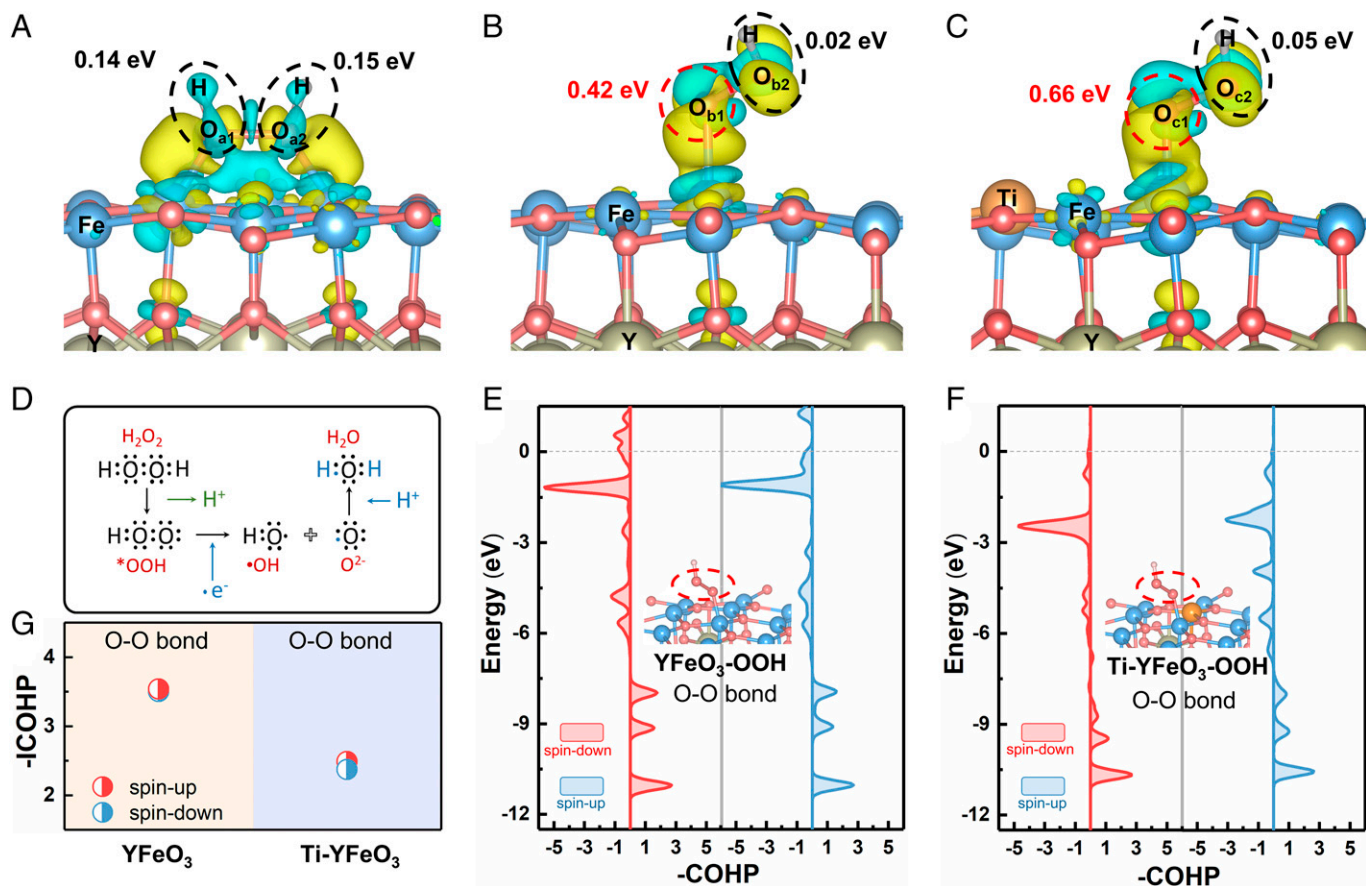


Fig. 2. Charge transfer behavior and molecular bond strength relationship. The different charge density of H_2O_2 adsorbed on YFeO_3 (A), $\bullet\text{OOH}$ adsorbed on YFeO_3 (B), and Ti-YFeO_3 (C). Different adsorbed oxygen atoms were labeled as O_{a1} , O_{a2} , O_{b1} , O_{b2} , O_{c1} , and O_{c2} . The Bader charge corresponding to dashed box was recorded. The charge density of yellow and blue represents the concentrated and scarce electrostatic potential scale respectively. (D) Electron transfer process in the formation of $\bullet\text{OH}$ by H_2O_2 activation. COHP of $\text{YFeO}_3\text{-OOH}$ (E) and $\text{Ti-YFeO}_3\text{-OOH}$ (F). (G) The corresponding ICOHP in E and F.

of Fe(II) was found from the high-resolution XPS spectra of Fe 3p (Fig. 3A). Fig. 3B showed the calculated density of states for YFeO_3 and Ti-YFeO_3 , which attested that the Fe(II) states appeared after Ti modification. The Fe(II) state was existing as a small polaron state caused by the interaction of the Fe 3p and Ti 3p region, which was most likely a localized Fe ion 3d-derived state introduced by Ti modification (41). In order to further understand the changes in the local coordination structure of the catalyst after modification, X-ray absorption fine structure spectroscopy (XAFS) was performed (Fig. 3C–G). As shown in the X-ray absorption near edge structure (XANES) curves of the Fe K-edge (Fig. 3C), the absorption edge position of Ti-YFeO_3 shifted toward lower energy than that of YFeO_3 , demonstrating that the average valance state of Fe ions in Ti-YFeO_3 decreased, which was the result of a charge transfer (42, 43). It will be more conducive to the charge transfer between the catalyst and H_2O_2 molecules, which is consistent with above theoretical results (Fig. 2B and C). The Fourier-transform extended X-ray absorption fine structure (FT-EXAFS) spectra (Fig. 3D) of YFeO_3 and Ti-YFeO_3 exhibited two peaks at $\sim 1.6 \text{ \AA}$ and 3.4 \AA , which may be attributed to the Fe–O bond and Fe–O–Fe bond, respectively (42). Compared with the peaks of Fe foil and FeO, they were more similar to those of Fe_2O_3 . Fig. 3G showed the wavelet transform (WT) analysis of YFeO_3 , Ti-YFeO_3 , Fe_2O_3 , and Fe foil (43). To further investigate the coordination configuration and the chemical bond length change, the FT-EXAFSs were fitted (Fig. 3F and SI Appendix, Table S1). The Fe–O coordination number of the YFeO_3 catalyst increased slightly after Ti

modification, meaning that there would be more coordination sites for Fe atoms at the surface of Ti-YFeO_3 . In the heterogeneous reaction, these may be able to become reaction active sites to provide more coordination opportunities between catalysts and reaction molecules. The Fe–O bond length of the YFeO_3 catalyst had also increased, resulting in an increase for the Fe–O–Fe bond length, as shown in Fig. 3E. Furthermore, the plane where the Fe atoms were located would also be offset in the horizontal or vertical direction, which was called surface relaxation (44). The above-mentioned changes in coordination structure and bond length were derived from the surface relaxation caused by Ti modification. Significantly, such an increase in the Fe–Fe space would cause the coordination molecule to be stretched more severely when the coordination molecule was coordinating with Fe sites, so that the absorbed molecules become more active (45).

Effect of Surface Relaxation on Fenton-Like Performance. In order to further confirm the effect of surface relaxation on H_2O_2 activation, the Fenton-like (photo-Fenton) reaction behavior of YFeO_3 and Ti-YFeO_3 was investigated, using 4-chloro phenol (4-CP) and RhB as model compounds. After regulating the surface relaxation of catalysts, the degradation efficiencies of Ti-YFeO_3 obtained obvious improvement compared with those of YFeO_3 , and the removal rate and reaction kinetic of 3% Ti-doped YFeO_3 reached the maximum of them (SI Appendix, Figs. S11 and S12). The reaction kinetic constant (k) for the $\text{Ti-YFeO}_3/\text{H}_2\text{O}_2/\text{light}$ system was ~ 3 times greater than that of the $\text{YFeO}_3/\text{H}_2\text{O}_2/\text{light}$ system for the Fenton-like catalytic

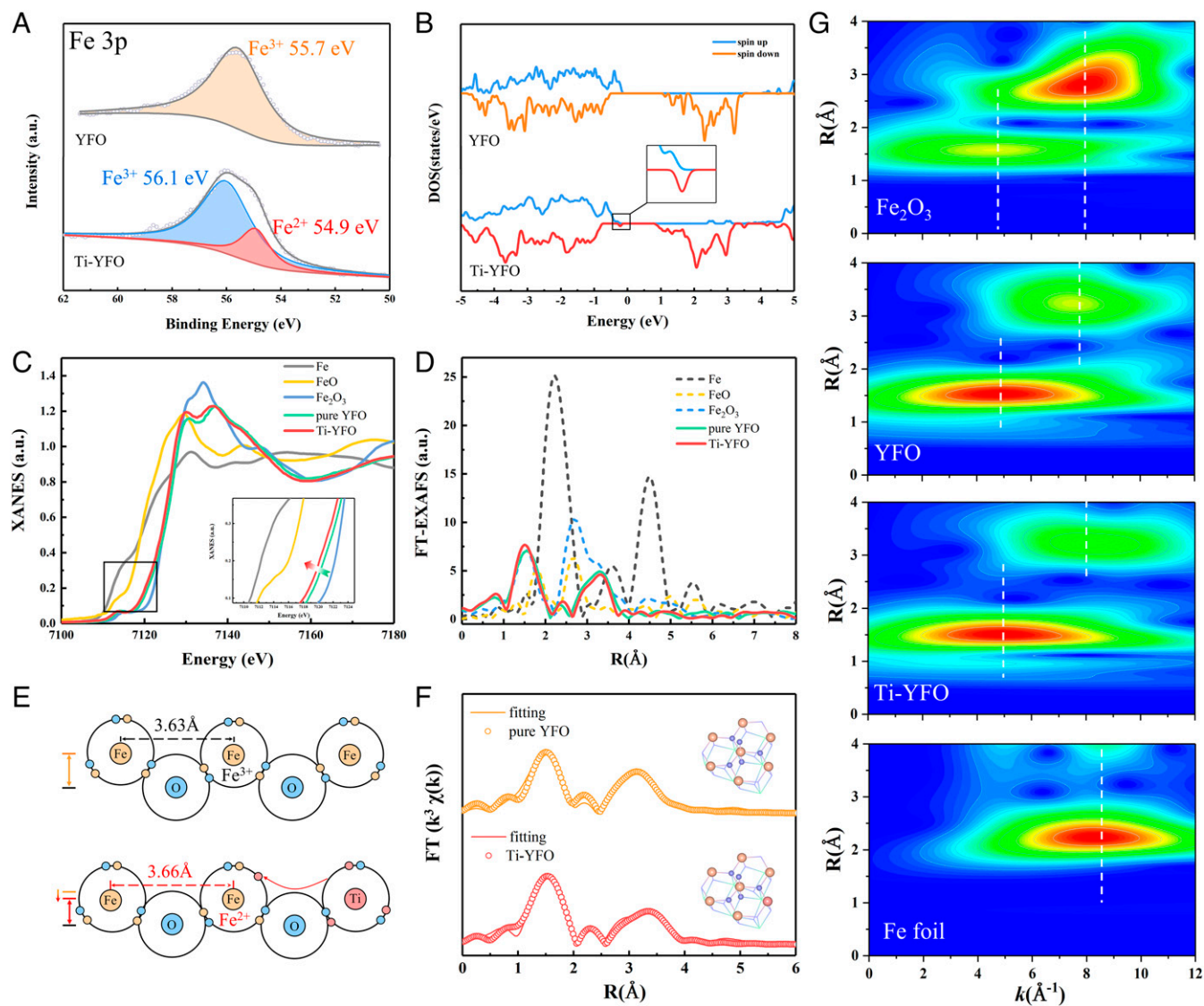
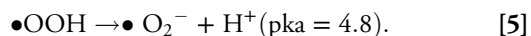


Fig. 3. Structure characterization of catalysts. (A) XPS spectra of Fe 3p for YFeO_3 and Ti-YFeO_3 . (B) Calculated projected density of states using DFT + U for Fe 3d orbitals. Normalized Fe K-edge XANES (C) and Fourier-transformed (FT) (D) curves at R space of Fe foil, FeO , Fe_2O_3 , YFeO_3 , and Ti-YFeO_3 . (E) Schematic diagram of charge transfer and local structure change after modification. (F) The corresponding EXAFS spectra along with fits of YFeO_3 and Ti-YFeO_3 . (G) WT contour plots of $k(2)$ -weighted $\chi(k)$ signals from Fe foil, Fe_2O_3 , YFeO_3 , and Ti-YFeO_3 .

oxidative degradation, indicating the beneficial effect of surface relaxation. Similarly, its degradation ability of 4-CP and AR also reached a high level (Fig. 4A and *SI Appendix*, Fig. S13). The three-dimension excitation emission matrix fluorescence spectroscopy (3D-EEM) in the *SI Appendix*, Fig. S16 indicated that 4-CP was almost completely removed after the degradation reaction for 3 h. Its total organic carbon (TOC) removal value (Fig. 4B) reached up to 82% after the irradiation. Furthermore, YFeO_3 modified with Ti doping owned perfect pollutant removal abilities at various pH values (Fig. 4C), which broadened its application scenarios. Moreover, the chemical stability of Ti-YFeO_3 was monitored over multiple runs (*SI Appendix*, Fig. S17), and we did not detect Fe ion leaching (*SI Appendix*, Fig. S18). The Fourier translation infrared spectroscopy (FT-IR) and XRD patterns (*SI Appendix*, Fig. S19) before and after the reaction proved that pollutants had no residue on the surface and indicated the structural stability of Ti-YFeO_3 .

In Fenton-like processes, the tracing of active free radicals was very important. The involved reactive species were identified by radical scavenging tests and electron paramagnetic resonance

(EPR) analysis. Nevertheless, the semiquantitative detection of the $\bullet\text{OOH}$ radical was difficult to achieve for the time being. We focused on $\bullet\text{OH}$ free radicals derived from the transformation of $\bullet\text{OOH}$ radicals and the other $\bullet\text{O}_2^-$ free radicals. The main production path of the $\bullet\text{O}_2^-$ free radical was in Eq. 5. In Eq. 5, $\bullet\text{OOH}$ species may come from a small amount of desorption of $\bullet\text{OOH}$ radicals:



Using p-benzoquinone as the scavenger of $\bullet\text{O}_2^-$ radicals, the removal rate in the $\text{Ti-YFeO}_3/\text{H}_2\text{O}_2/\text{light}$ system remained at a relatively high level (Fig. 4D). In contrast, using tert-butyl alcohol (TBA) as the scavenger of $\bullet\text{OH}$ radicals, the removal rate had a noticeable drop, indicating a primary role of $\bullet\text{OH}$ radicals in the pollutant degradation (46). The contributions of $\bullet\text{OH}$, $\bullet\text{O}_2^-$, and others were calculated according to Eqs. 6–8, respectively. The $\bullet\text{OH}$ radicals accounted for 90.7% of the contribution to the Fenton-like reaction. 5,5-dimethyl-1-pyrroline N-oxied (DMPO) $-\bullet\text{O}_2^-$ and DMPO- $\bullet\text{OH}$ were detected

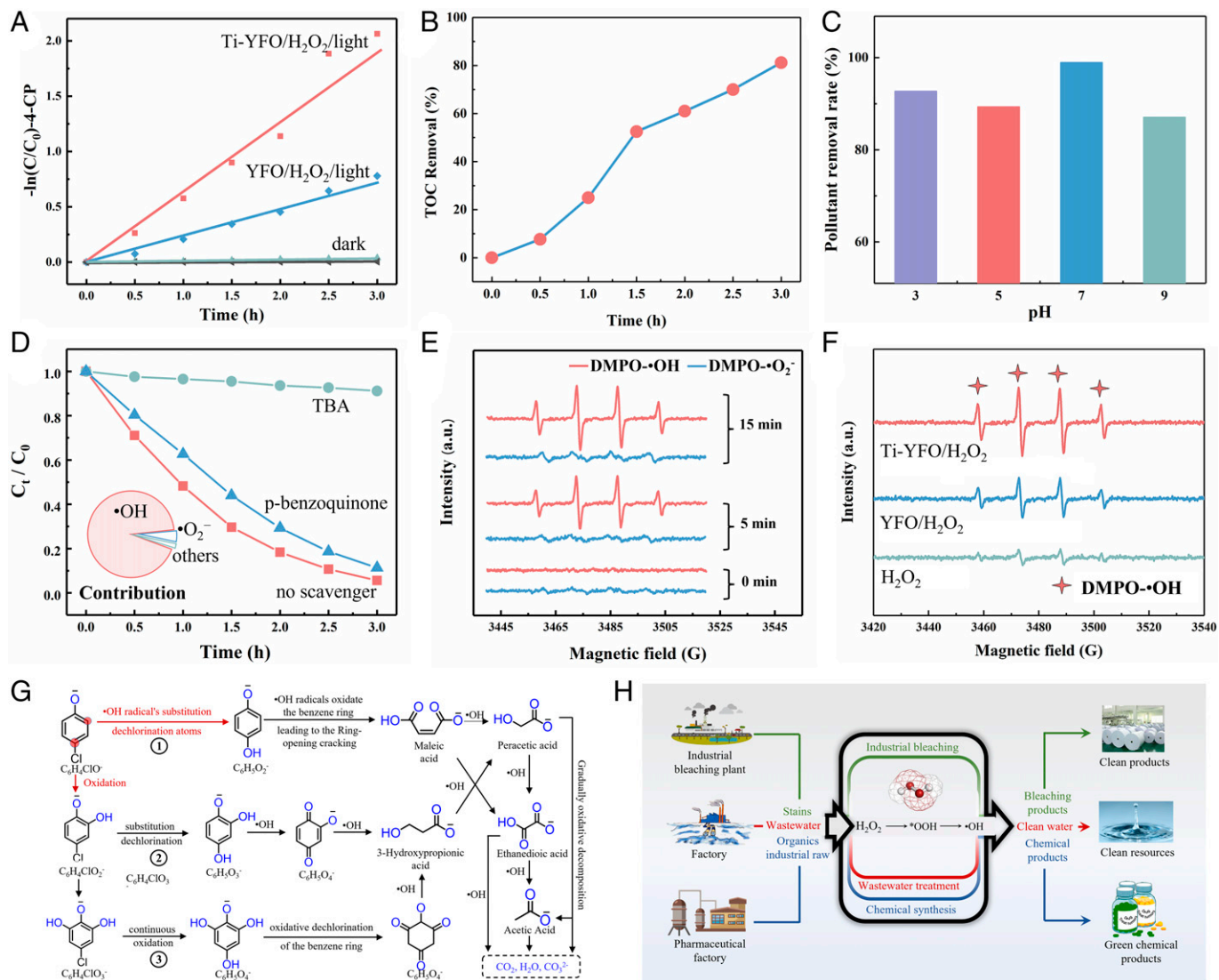


Fig. 4. Photo-Fenton performance in different systems. (A) The corresponding Langmuir–Hinshelwood kinetics plots of 4-CP. (B) TOC change in Ti-YFeO₃ system. (C) Removal efficiencies at different pH values. (D) Removal efficiencies with TBA (the •OH scavenger) and p-benzoquinone (the •O₂⁻ scavenger). The illustration shows the contribution of different active radicals to the reaction. (E) EPR spectra of DMPO-•O₂⁻ and DMPO-•OH as a function of time (a.u.: arbitrary unit). (F) DMPO-•OH for different systems after 15-min visible light irradiation. (G) •OH free radical activity mechanism and molecular transformation pathways of 4-CP. (H) Wide application prospects of H₂O₂ molecules.

by EPR along with time (Fig. 4E). The amount of •OH radicals increased with time, while that of •O₂⁻ did not increase significantly. This further supported the conclusion that •OH radicals were the main active species. The presence of •O₂⁻ free radicals also confirmed that there were *OOH radicals in this system. The intensity of the Raman signal peak was often positively correlated with the number of corresponding species. As shown in *SI Appendix, Fig. S20*, by observing the relative intensity of the two peaks (Fe-OOH 632 cm⁻¹ and Fe-OH 563 cm⁻¹), the relative intensity of the Ti-YFeO₃ catalyst was stronger than that of YFeO₃, indicating Ti-YFeO₃ had a stronger ability to produce *OOH species. In addition, as shown in Fig. 4F, the EPR signals of DMPO-•OH became stronger after YFeO₃ was modified with Ti doping (36). And the EPR signal of DMPO-•O₂⁻ was not significantly enhanced (*SI Appendix, Fig. S21*). The higher signal intensity of •OH in a short time illustrated that surface relaxation caused by Ti modification effectively promoted this critical step reaction rate in the Fenton-like system. This was beneficial to the activation process of H₂O₂ molecules, improving the generation efficiency of •OH radicals, thus promoting

the Fenton-like reaction rate. In addition, as shown in *SI Appendix, Figs. S4B and S11D*, the conductivity of 5% Ti-doped YFeO₃ was significantly higher than that of 3% Ti-doped YFeO₃. However, in the test of the photo-Fenton reaction, 5% Ti-doped YFeO₃ had worse Langmuir–Hinshelwood kinetics than 3% Ti-doped YFeO₃. This further indicated that the improvement in the H₂O₂ activation ability did not mainly come from the increase of conductivity but from the improvement of local coordination environment and charge. Furthermore, the proposed molecular transformation pathways of 4-CP were inferred (Fig. 4G), combined with electrospray high-resolution mass spectrometry analysis (*SI Appendix, Figs. S22 and S23*) in negative ion mode. In addition, H₂O₂ holds promise for wider applications, such as green chemical synthesis (Fig. 4H). The strategy of surface relaxation provides an idea for realizing efficient applications.

Theoretical Study on Activation Kinetics of H₂O₂ Molecules.

DFT calculations were employed to gain insight into the decomposition pathways of H₂O₂ and investigate the mechanism of surface relaxation action. Here, the traditional decomposition path

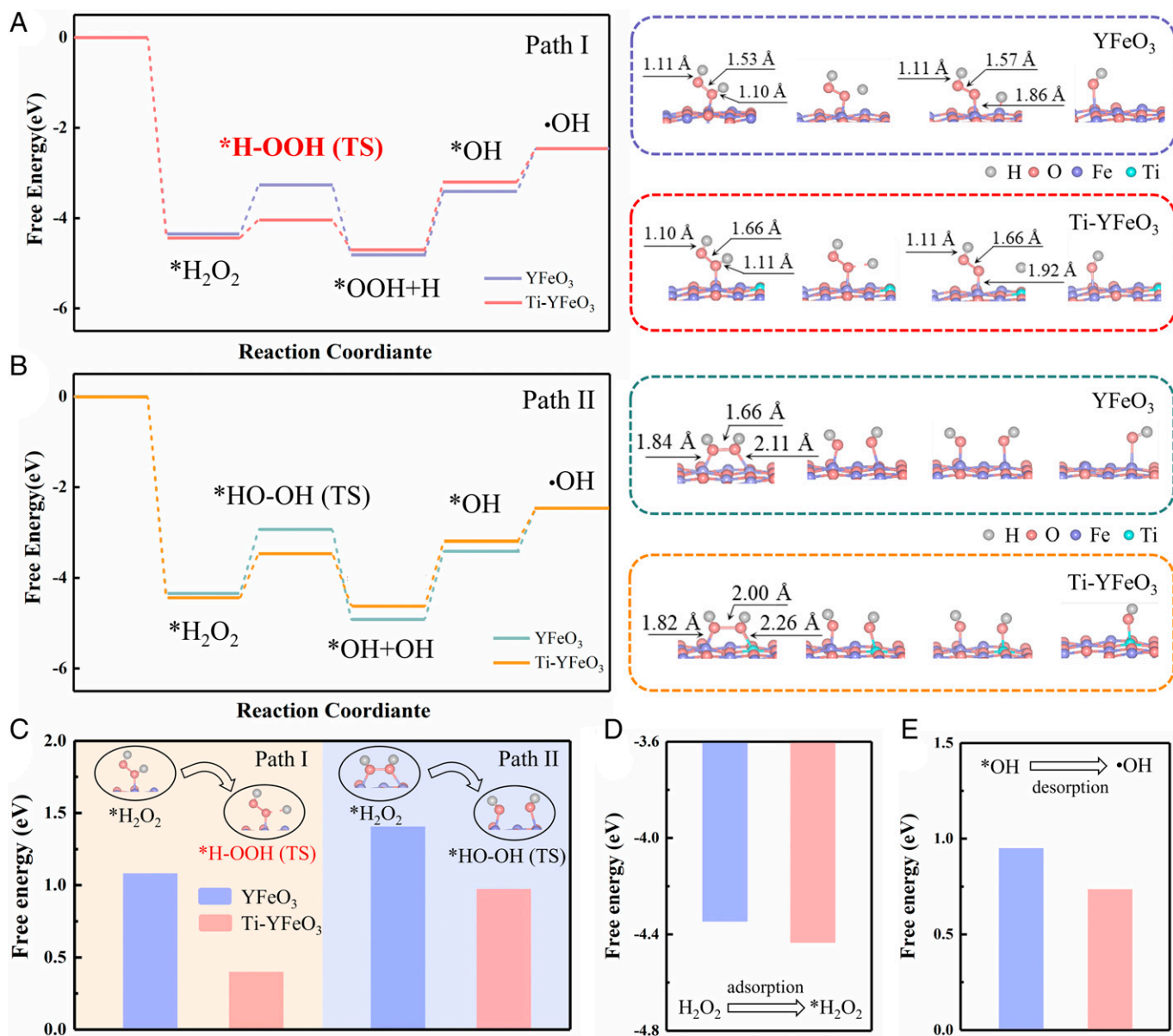


Fig. 5. DFT calculations. Calculated free energy profiles for path I: YFeO₃ (purple), Ti-YFeO₃ (red) (A); path II: YFeO₃ (green), Ti-YFeO₃ (yellow) (B). The boxes on the *Right* are schematic representations of H₂O₂ photoactivation processes for path I and path II. (C) The activation from *H₂O₂ to *H-OOH (TS) or *HO-OH (TS) for path I or path II. The adsorption of H₂O₂ (D) and desorption of *OH (E) (blue, YFeO₃; red, Ti-YFeO₃).

was also listed as a comparison. The most favorable configurations were shown in Fig. 5 and *SI Appendix, Fig. S24*, which have proceeded by two contrasting coordination methods, as follows: single oxygen coordination (path I) and dioxygen coordination (path II). And the corresponding Gibbs free energy dates for the two paths were shown in *SI Appendix, Table S2*. For path I, H₂O₂ was adsorbed to a Fe atom via a single Fe-O coordination and transformed to *OOH (Fe-OOH) with breaking of the O-H bond. Then, the peroxy bond was broken under the shock to generate •OH or *OH (Fig. 5A). For path II, H₂O₂ was adsorbed to two Fe atoms via double Fe-O coordination and translated to *OH with the breaking of the peroxy bond (Fig. 5B), which was a traditional and widely reported path. The corresponding Gibbs free energy (−3.262 eV) for forming *H-OOH(TS) in path I was lower than that (−2.935 eV) for *HO-OH(TS) in path II, indicating the production of *H-OOH(TS) was more favorable (Fig. 5C). The low free energy of intermediate formation for path I indicated that it had

the possibility of being dominant in the H₂O₂ decomposition process, which was consistent with the SHINERS results.

The mechanism of the effect of Ti modification was further investigated. For path I, *SI Appendix, Fig. S25* showed that the H₂O₂ adsorption energies of three different sites (Fe sites at pure YFeO₃, Fe sites and Ti sites at Ti-YFeO₃) were significantly different. Compared with Fe sites at pure YFeO₃ or Ti-YFeO₃, Ti sites were not conducive to the adsorption of H₂O₂, which made them lack the ability for the further activation of H₂O₂. However, as the electron donor sites, Ti sites played the role of activating Fe active sites and participated in the activation process of H₂O₂. Due to the differences in local microenvironment, peroxy bonds (1.66 Å) and O-H bonds (1.11 Å) of the catalyst with Ti modification were longer than peroxy bonds (1.57 Å) and O-H bonds (1.10 Å) of pure catalysts (Fig. 5A), respectively, leading to easier fracture for O-H bonds of adsorbed H₂O₂ and peroxy bonds of *OOH in the subsequent process. The corresponding Gibbs free energy

(−4.032 eV) of Ti-YFeO₃ for forming *H-OOH(TS) was obviously lower than that of the pure catalyst (−3.262 eV), which was extremely beneficial for the decomposition of H₂O₂. As shown in the calculated free energy profiles, the adsorption of H₂O₂ and the desorption of *OH became more favorable due to the improvement of the local coordination environment of the catalyst by Ti modification (Fig. 5 D and E). The favorable desorption of *OH would promote the continued adsorption of H₂O₂ or the adsorption and activation of pollutant molecules by the catalyst, thereby promoting the progress of the entire reaction, rather than occupying active sites to make subsequent processes impossible. Therefore, it was obvious that surface relaxation was very advantageous for the photoactivation of H₂O₂ molecules, and it would enhance the ability to generate active free radicals, further increasing the reaction kinetics rate. This strategy was not only applicable to path I but also beneficial to the traditional path II.

Discussion

In summary, this study gave a perspective for understanding the photoactivation mechanism of H₂O₂. Sufficient evidence for *OOH as the intermediate species was provided by in situ SHINERS, isotope labeling, and DFT calculations. The surface relaxation of YFeO₃ catalysts by Ti modification can facilitate the photoactivation of H₂O₂ molecules and accelerate the production of *OOH species, which increased the production rate of •OH radicals by several times. As a result, the pollutant removal rate of Ti-doped YFeO₃ was 3 times than that of YFeO₃ during the process of photo-Fenton reaction. This study may provide ideas for designing catalysts applied in heterogeneous Fenton-like reactions.

Materials and Methods

Synthesis of YFeO₃. Y(NO₃)₃•6H₂O, Fe(NO₃)₃•9H₂O, C₆H₁₈N₂O₈Ti [dihydroxybis (ammonium lactate) titanium(IV)] and C₆H₈O₇•H₂O were fed according to the molar ratio of 1: (1-x): x: 4. The reagent was dissolved in 120 mL deionized water and stirred intensely. The solution was placed in an oil bath pot heated to 75 °C and stirred continuously for 4 h. The oil bath temperature was raised to 120 °C and kept until the water was completely evaporated. After that, the obtained gel was placed into the oven at 120 °C for 12 h. The obtained powders were heated in the muffle furnace at 450 °C for 3 h and were then fully ground and were finally calcined at 730 °C for 3 h. YFeO₃ powders with different Ti doping ratios were obtained.

Characterization. XRD measurements were performed with a Rigaku Ultima III X-ray diffractometer (Cu K α radiation, 40 kV and 40 mA) in the range of 10 to 80° (2 theta). The instrument employed for XPS measurements was Perkin-Elmer PHI 5000C, and all binding energies were calibrated with C1s at 284.6 eV. The morphology of as-prepared samples was examined by a scanning electron microscope (SEM; Hitachi S3400N II). TEM was conducted on a transmission electron microscope (JEOL-JEM 200CX) operated at 200 kV. HAADF and ABF images were acquired with a FEI Titan G² 80-200 ChemiSTEM with a spherical aberration corrector working at 200 kV. The EPR spectra were recorded with a Bruker EMX 10/12 X-band spectrometer. The diffuse reflectance spectra were measured on an ultraviolet-visible-near-infrared (UV-Vis-NIR) spectrophotometer (UV-LAMBDA 950; PerkinElmer). FT-IR NEXUS870 was used to characterize the chemical bonds of the samples. The specific surface area of as-prepared samples was measured by an automatic surface area analyzer (Micromeritics ASAP 2020) from the adsorption branch of N₂ isotherm, and the pore size distribution was calculated from Barrett-Joyner-Halenda method for mesopores. The total iron content of the solution was detected the atomic absorption spectrometer (AAS, 180-80, Hitachi). The Raman spectra were characterized with confocal laser Raman spectrometers (Horiba, LabRAM Aramis; Witec Alpha 300, calibrated with silicon). The X-ray absorption near edge structure (XANES) experiment was carried out at Beijing

Synchrotron Radiation Facility (BSRF). Data of XAFS were processed using the Athena and Artemis programs of three IFEFFIT packages based on FEFF 6. Data were processed with k (3) weighting and an Rbkg value of 1.0. Normalized extended XAFS (EXAFS) data were obtained directly from the Athena program of the IFEFFIT package.

Before electronic measure and photoelectronic measure, it was firstly made to YFO film by the electrophoretic deposition (EPD) method. The electrolyte was a 0.5 M Na₂SO₄ solution. The frequency of the Mott-Schottky measure is using 500 HZ. The i-t curve was measured at 1.23 V versus reversible hydrogen electrode (RHE).

Measurement of In Situ SHINERS. First, to facilitate testing, the YFO catalyst films were obtained by EPD methods. The wavelength of the excitation laser was 488 nm (the power was ~5 mW). Raman frequencies were calibrated using a Si wafer. Each Raman spectrum shown here was acquired over a collection time of 100 s and the average of two measurements.

Measurement of Fenton-Like Reaction. The Fenton-like (photo-Fenton) measurement of photocatalytic experiments was carried out in a photoreactor by degradation of dyes (RhB, AR) under visible-light irradiation equipped with a 300-W Xe arc lamp with an UV cutoff filter ($\lambda > 420$ nm). The obtained experiments were added in aqueous solution of dye (100 mL, 20 mg L⁻¹) and H₂O₂ (0.4 M) with constant string for 1 h to establish an adsorption-desorption equilibrium. The pH value of the solution is ~4. At the given time intervals for 30 min, ~3 mL of the suspension was taken for further analysis by a syringe equipped with a filter. The contents of dyes including RhB and AR were analyzed by UV-Vis-NIR spectroscopy. Degradation efficiency is equal to C/C₀, where C₀ was the initial dye concentration and C was the instant dye concentration. The pseudofirst-order kinetic model is obtained by $-\ln(C/C_0)$. EPR was used to examine the photodegradation mechanism by detecting reactive radicals. A •O₂⁻ radical was captured by DMPO to form DMPO•O₂⁻ in the methanol solution system and then it was detected by EPR. Similarly, DMPO•OH was formed in the water solution system, to be detected. The dissolved ferrous ions and total iron ions were quantified by the 1, 10-phenanthroline method and analyzed at a maximum wavelength of 510 nm with a UV-Vis-NIR spectrophotometer. The TOC concentration of the degradation agent was recorded using an ELEMENTAR, vario TOC. Using a 60-mg catalyst, the degradation of 4-CP (3 mg L⁻¹) was carried out. The concentration of 4-CP was measured by the 4-aminoantipyrine method. 3D-EEM spectra of the 4-CP sample were measured by using a luminescence spectrometer (LS-55; PerkinElmer Co.) The liquid chromatography-mass spectrometry (LC-MS) was measured by Dionex Ultimate 3000 ultra-high-performance liquid chromatography-Thermo Scientific Q Exactive. The chromatographic column is Eclipse Plus C18 (100 mm × 4.6 mm, 5 μ m) and the ion source is HESI. We further determined the contribution from •OH and •O₂⁻ quantitatively. The reaction rate constants after adding TBA and p-benzoquinone were denoted as k₁ and k₂, respectively, and the initial rate constant without quenching agent was k₀. The contributions of •OH, •O₂⁻ and others were calculated according to Eqs. 6-8 (17):

$$\lambda(\bullet\text{OH}) = [(k_0 - k_1)/k_0] \times 100\%, \quad [6]$$

$$\lambda(\bullet\text{O}_2^-) = [(k_0 - k_2)/k_0] \times 100\%, \quad [7]$$

$$\lambda(\text{others}) = 1 - \lambda(\bullet\text{OH}) - \lambda(\bullet\text{O}_2^-), \quad [8]$$

where $\lambda(\bullet\text{OH})$, $\lambda(\bullet\text{O}_2^-)$, and $\lambda(\text{others})$ were the contributions of •OH, •O₂⁻ and others in the reaction process, respectively.

Computational Details.

Free energy calculation. We have employed the first principles (47, 48) to perform all spin-polarization DFT calculations within the generalized gradient approximation (GGA) using the Perdew-Burke-Ernzerhof (PBE) (49) formulation. The DFT calculations in this study are performed using the VASP code. We have chosen the projected augmented wave (PAW) potentials (50, 51) to describe the ionic cores and take valence electrons into account using a plane wave basis set with a kinetic energy cutoff of 400 eV. Partial occupancies of the Kohn-Sham orbitals were allowed using the Gaussian smearing method and a width of 0.05 eV. The electronic energy was considered self-consistent when the energy change was smaller than 10⁻⁶ eV. A geometry optimization was considered convergent when the energy change was smaller than 0.05 eV Å⁻¹. In our structure, the U

correction is used for Y and Fe atoms. The vacuum spacing in a direction perpendicular to the plane of the structure is 15 Å for the YFeO₃ (001) surfaces. The Brillouin zone integration is performed using 3 × 3 × 1 Monkhorst-Pack k-point sampling for a structure. Finally, the adsorption energies (E_{ads}) were calculated as $E_{\text{ads}} = E_{\text{ad/sub}} - E_{\text{ad}} - E_{\text{sub}}$, where $E_{\text{ad/sub}}$, E_{ad} , and E_{sub} are the total energies of the optimized adsorbate/substrate system, the adsorbate in the structure, and the clean substrate, respectively. The free energy was calculated using the Eq. 9:

$$G = E_{\text{ads}} + \text{ZPE} - \text{TS}, \quad [9]$$

where G , E_{ads} , ZPE, and TS are the free energy, total energy from DFT calculations, zero point energy, and entropic contributions, respectively.

The Bader charge, COHP had been calculated using the first principles. In addition, the charge density was analyzed by the VESTA package.

DOS calculation. Our total energy and electronic structure calculations were performed using the plane-wave pseudopotential techniques with the GGA in the PBE parametrization, with spin-polarized effects considered. The strong on-site Coulomb repulsion between localized 3d electrons was modified by considering the Hubbard U correction proposed by Dudarev et al., and the effective U value of 5.3 eV was used for Fe 3d orbitals (52). The cutoff energy for the plane-wave basis set was chosen to be 520 eV and a Monkhorst-Pack k-point grids of 4 × 4 × 2 was used for Brillouin zone integration.

Raman frequencies calculation. The first simulation software package used in this work was VASP (53). Low-frequency (from 550 to 730 cm⁻¹) Raman spectra of OOH on the Fe site of YFeO₃ substrate were calculated based on the DFT

method within the GGA. The PAW potentials were adopted for inner electrons (51). PBE functional was used for exchange-correlation potential (49). For the lattice optimization, the kinetic energy cutoff was chosen as 400 eV for the wave function. The Monkhorst-Pack method was used to sample the density at k-point (54). The limit of energy convergence was 10⁻⁸ eV, and the convergence condition for the maximum atomic force was 0.01 eV Å⁻¹. Grimme's DFT-D3 methodology (55) was used to describe the dispersion interactions among all the atoms in adsorption models of interest.

Data, Materials, and Software Availability. All study data are included in the article and/or *SI Appendix*.

ACKNOWLEDGMENTS. This work was supported by the National Key Research and Development Program of China (Grant No. 2018YFA0209303), the National Natural Science Foundation of China (Grant Nos. 22025202, 51972165), and the Natural Science Foundation of Jiangsu Province of China (Grant No. BK20202003). The numerical calculations in this paper were carried out on the supercomputing system of the Supercomputing Center of Nanjing University.

Author affiliations: ^aCollaborative Innovation Center of Advanced Microstructures, National Laboratory of Solid State Microstructures, College of Engineering and Applied Sciences, Nanjing University, Nanjing 210093, China; ^bJiangsu Key Laboratory of Nano Technology, Nanjing University, Nanjing 210093, China; and ^cCollege of Mechanics and Materials, Hohai University, Nanjing 210098, China

- S. S. Gupta et al., Rapid total destruction of chlorophenols by activated hydrogen peroxide. *Science* **296**, 326–328 (2002).
- S. C. Perry et al., Electrochemical synthesis of hydrogen peroxide from water and oxygen. *Nat. Rev. Chem.* **3**, 442–458 (2019).
- C. Dong, J. Ji, B. Shen, M. Xing, J. Zhang, Enhancement of H₂O₂ Decomposition by the co-catalytic effect of WS₂ on the Fenton reaction for the synchronous reduction of Cr(VI) and remediation of phenol. *Environ. Sci. Technol.* **52**, 11297–11308 (2018).
- Z. Yang, J. Qian, A. Yu, B. Pan, Singlet oxygen mediated iron-based Fenton-like catalysis under nanoconfinement. *Proc. Natl. Acad. Sci. U.S.A.* **116**, 6659–6664 (2019).
- W. Wu, Y. Pu, H. Lin, H. Yao, J. Shi, Starvation-sensitized and oxygenation-promoted tumor sonodynamic therapy by a cascade enzymatic approach. *Research (Wash D C)* **2021**, 9769867 (2021).
- Y. Zhu et al., Strategies for enhancing the heterogeneous Fenton catalytic reactivity: A review. *Appl. Catal. B* **255**, 117739 (2019).
- Y. Shang, X. Xu, B. Gao, S. Wang, X. Duan, Single-atom catalysis in advanced oxidation processes for environmental remediation. *Chem. Soc. Rev.* **50**, 5281–5322 (2021).
- X. Zhou et al., Identification of Fenton-like active Cu sites by heteroatom modulation of electronic density. *Proc. Natl. Acad. Sci. U.S.A.* **119**, e2119492119 (2022).
- S. Gligorovski, R. Strekowski, S. Barbat, D. Vione, Environmental implications of hydroxyl radicals *OH. *Chem. Rev.* **115**, 13051–13092 (2015).
- S. E. Paulson et al., A light-driven burst of hydroxyl radicals dominates oxidation chemistry in newly activated cloud droplets. *Sci. Adv.* **5**, eaav7689 (2019).
- L. Chen et al., Selective interfacial oxidation of organic pollutants in Fenton-like system mediated by Fe(III)-adsorbed carbon nanotubes. *Appl. Catal. B* **292**, 120193 (2021).
- Y. Zhang et al., Photoinduced uptake and oxidation of SO₂ on Beijing urban PM_{2.5}. *Environ. Sci. Technol.* **54**, 14868–14876 (2020).
- C. Miller et al., Kinetic analysis of H₂O₂ activation by an iron(III) complex in water reveals a nonhomolytic generation pathway to an iron(IV)oxo complex. *ACS Catal.* **11**, 787–799 (2021).
- J. Xu et al., Organic wastewater treatment by a single-atom catalyst and electrolytically produced H₂O₂. *Nat. Sustain.* **4**, 233–241 (2021).
- L. Ding et al., The vital role of surface Brønsted acid/base sites for the photocatalytic formation of free ·OH radicals. *Appl. Catal. B* **266**, 118634 (2020).
- Y. Zhang et al., Heterogeneous degradation of organic contaminants in the photo-Fenton reaction employing pure cubic β-Fe₂O₃. *Appl. Catal. B* **245**, 410–419 (2019).
- L. S. Zhang et al., Carbon nitride supported high-loading Fe single-atom catalyst for activation of peroxydisulfate to generate ¹O₂ with 100% selectivity. *Angew. Chem. Int. Ed. Engl.* **60**, 21751–21755 (2021).
- Y. Shi et al., Visible light promoted Fe₃S₄ Fenton oxidation of atrazine. *Appl. Catal. B* **277**, 119229 (2020).
- L. Shi et al., Multi-functional 3D honeycomb ceramic plate for clean water production by heterogeneous photo-Fenton reaction and solar-driven water evaporation. *Nano Energy* **60**, 222–230 (2019).
- R. Liu, Y. Xu, B. Chen, Self-assembled nano-FeO(OH)/reduced graphene oxide aerogel as a reusable catalyst for photo-Fenton degradation of phenolic organics. *Environ. Sci. Technol.* **52**, 7043–7053 (2018).
- J. Li, C. Xiao, K. Wang, Y. Li, G. Zhang, Enhanced generation of reactive oxygen species under visible light irradiation by adjusting the exposed facet of FeWO₄ nanosheets to activate oxalic acid for organic pollutant removal and Cr(VI) reduction. *Environ. Sci. Technol.* **53**, 11023–11030 (2019).
- F. Chen et al., Molecular engineering toward pyrrolic N-rich M-N_x (M = Cr, Mn, Fe, Co, Cu) single-atom sites for enhanced heterogeneous Fenton-like reaction. *Adv. Funct. Mater.* **31**, 2007877 (2021).
- L. Su, P. Wang, X. Ma, J. Wang, S. Zhan, Regulating local electron density of iron single sites by introducing nitrogen vacancies for efficient Photo-Fenton process. *Angew. Chem. Int. Ed. Engl.* **60**, 21261–21266 (2021).
- Q. Yan et al., Constructing an acidic microenvironment by MoS₂ in heterogeneous Fenton reaction for pollutant control. *Angew. Chem. Int. Ed. Engl.* **60**, 17155–17163 (2021).
- H. Zeng et al., pH-independent production of hydroxyl radical from atomic H⁺-mediated electrocatalytic H₂O₂ reduction: A green Fenton process without byproducts. *Environ. Sci. Technol.* **54**, 14725–14731 (2020).
- J. Wang, J. Tang, Fe-based Fenton-like catalysts for water treatment: Catalytic mechanisms and applications. *J. Mol. Liq.* **332**, 115775 (2021).
- M. Zong et al., Facet-dependent photodegradation of methylene blue by hematite nanoparticles in visible light. *Environ. Sci. Technol.* **55**, 677–688 (2021).
- A. Plauk, E. E. Stangland, J. A. Dumesic, M. Mavrikakis, Active sites and mechanisms for H₂O₂ decomposition over Pd catalysts. *Proc. Natl. Acad. Sci. U.S.A.* **113**, E1973–E1982 (2016).
- F. Liu et al., Supported atomically-precise gold nanoclusters for enhanced flow-through electro-Fenton. *Environ. Sci. Technol.* **54**, 5913–5921 (2020).
- H. Q. Zheng et al., Zr-based metal-organic frameworks with intrinsic peroxidase-like activity for ultradeep oxidative desulfurization: Mechanism of H₂O₂ decomposition. *Inorg. Chem.* **58**, 6983–6992 (2019).
- J. C. Dong et al., In situ Raman spectroscopic evidence for oxygen reduction reaction intermediates at platinum single-crystal surfaces. *Nat. Energy* **4**, 60–67 (2018).
- J. F. Li et al., Shell-isolated nanoparticle-enhanced Raman spectroscopy. *Nature* **464**, 392–395 (2010).
- C. Hu et al., Surface-enhanced Raman spectroscopic evidence of key intermediate species and role of NiFe dual-catalytic center in water oxidation. *Angew. Chem. Int. Ed. Engl.* **60**, 19774–19778 (2021).
- Y. Guo et al., A novel wide-spectrum response hexagonal YFeO₃ photoanode for solar water splitting. *RSC Advances* **7**, 18418–18420 (2017).
- M. Ismael et al., Synthesis of phase pure hexagonal YFeO₃ perovskite as efficient visible light active photocatalyst. *Catalysts* **7**, 326 (2017).
- H. Wang et al., Enhanced degradation of organic pollutants over Cu-doped LaAlO₃ perovskite through heterogeneous Fenton-like reactions. *Chem. Eng. J.* **332**, 572–581 (2018).
- K. L. Stone, R. K. Behan, M. T. Green, Resonance Raman spectroscopy of chloroperoxidase compound II provides direct evidence for the existence of an iron(IV)-hydroxide. *Proc. Natl. Acad. Sci. U.S.A.* **103**, 12307–12310 (2006).
- R. Y. N. Ho et al., Raman evidence for a weakened O–O bond in mononuclear low-spin iron(III)-hydroperoxides. *J. Am. Chem. Soc.* **121**, 264–265 (1999).
- J. Chen et al., H₂O₂ oxidation by Fe(III)-OOH intermediates and its effect on catalytic efficiency. *ACS Catal.* **8**, 9665–9674 (2018).
- T. K. Das, M. Couture, Y. Ouellet, M. Guertin, D. L. Rousseau, Simultaneous observation of the O–O and Fe–O₂ stretching modes in oxyhemoglobins. *Proc. Natl. Acad. Sci. U.S.A.* **98**, 479–484 (2001).
- C. M. Tian et al., Electronic structure, optical properties, and photoelectrochemical activity of Sn-doped Fe₂O₃ thin films. *J. Phys. Chem. C* **124**, 12548–12558 (2020).
- Y. Cao et al., Molten-salt-assisted thermal etching method to transform bulk Fe₂O₃ into Fe single atom catalysts for oxygen reduction reaction in Zn-air battery. *Chem. Eng. J.* **420**, 129713 (2021).
- Q. B. Yu et al., Z-scheme α-Fe₂O₃/g-C₃N₄ with the FeOC bond toward enhanced photocatalytic degradation. *Colloids Surf. A Physicochem. Eng. Asp.* **616**, 126269 (2021).
- W. Lin et al., Structural characterizations and electronic properties of Ti-doped SnO₂(110) surface: A first-principles study. *J. Chem. Phys.* **124**, 054704 (2006).

45. J. Ma *et al.*, Efficient photoelectrochemical conversion of methane into ethylene glycol by WO₃ nanobar arrays. *Angew. Chem. Int. Ed. Engl.* **60**, 9357–9361 (2021).
46. X. Qian *et al.*, FeOOH quantum dots coupled g-C₃N₄ for visible light driving photo-Fenton degradation of organic pollutants. *Appl. Catal. B* **237**, 513–520 (2018).
47. G. Kresse, J. Furthmüller, Efficiency of ab-initio total energy calculations for metals and semiconductors using a plane-wave basis set. *Comput. Mater. Sci.* **6**, 15–50 (1996).
48. G. Kresse, J. Furthmüller, Efficient iterative schemes for ab initio total-energy calculations using a plane-wave basis set. *Phys. Rev. B Condens. Matter* **54**, 11169–11186 (1996).
49. J. P. Perdew, K. Burke, M. Ernzerhof, Generalized gradient approximation made simple. *Phys. Rev. Lett.* **77**, 3865–3868 (1996).
50. P. E. Blöchl, Projector augmented-wave method. *Phys. Rev. B Condens. Matter* **50**, 17953–17979 (1994).
51. G. Kresse, D. Joubert, From ultrasoft pseudopotentials to the projector augmented-wave method. *Phys. Rev. B* **59**, 1758–1775 (1999).
52. S. L. Dudarev, G. A. Botton, S. Y. Savrasov, C. J. Humphreys, A. P. Sutton, Electron-energy-loss spectra and the structural stability of nickel oxide: An LSDA+U study. *Phys. Rev. B* **57**, 1505–1509 (1998).
53. X. F. Shi *et al.*, Main reinforcement effects of precipitation phase Mg₂Cu₂Si, Mg₂Si and MgCu₂ on Mg-Cu-Si alloys by ab initio investigation. *Physica B* **521**, 339–346 (2017).
54. D. J. Chadi, Special points for Brillouin-zone integrations. *Phys. Rev. B* **16**, 5188–5192 (1977).
55. S. Grimme, J. Antony, S. Ehrlich, H. Krieg, A consistent and accurate ab initio parametrization of density functional dispersion correction (DFT-D) for the 94 elements H-Pu. *J. Chem. Phys.* **132**, 154104 (2010).